Direct three-dimensional printing of polymeric scaffolds with nanofibrous topography

Direct three-dimensional printing of polymeric scaffolds with nanofibrous topography

Aruna Prasopthum, Kevin M. Shakesheff, and Jing Yang*

Division of Regenerative Medicine and Cellular Therapies, School of Pharmacy, University of Nottingham, Nottingham, NG7 2RD, United Kingdom.

*Corresponding author: Jing Yang (ORCID: 0000-0002-8822-7124), Division of Regenerative Medicine and Cellular Therapies, School of Pharmacy, University of Nottingham, Nottingham, NG7 2RD, United Kingdom, Tel and Fax: +441157484690, e-mail: jing.yang@nottingham.ac.uk

Abstract

Three-dimensional (3D) printing is a powerful manufacturing tool for making 3D structures with well-defined architectures for a wide range of applications. The field of tissue engineering has also adopted this technology to fabricate scaffolds for tissue regeneration. The ability to control architecture of scaffolds, e.g. matching anatomical shapes and having defined pore size, has since been improved significantly. However, the material surface of these scaffolds is smooth and does not resemble that found in natural extracellular matrix (ECM), in particular, the nanofibrous morphology of collagen. This natural nanoscale morphology plays a critical role in cell behaviour. Here, we have developed a new approach to directly fabricate polymeric scaffolds with an ECM-like nanofibrous topography and defined architectures using extrusion-based 3D printing. 3D printed tall scaffolds with interconnected pores were created with disparate features spanning from nanometres to centimetres. Our approach removes the need for a sacrificial mould and subsequent mould removal compared to previous methods. Moreover, the nanofibrous topography of the 3D printed scaffolds significantly enhanced protein absorption, cell adhesion and differentiation of human mesenchymal stem cells (MSCs)

when compared to those with smooth material surfaces. These 3D printed scaffolds with both defined architectures and nanoscale ECM-mimicking morphologies have potential applications in cartilage and bone regeneration.

Keywords: 3D printing, tissue engineering, poly(L-lactide), nanofibrous scaffolds, mesenchymal stem cells, differentiation

Abbreviations: MSCs, mesenchymal stem cells; PLLA, poly(L-lactide); 2D, two-dimensional; 3D, three-dimensional; ECM, extracellular matrix; ALP, alkaline phosphatase; TIPS, thermally-induced phase separation; nHA, hydroxyapatite nanoparticles; CAD, computer-aided design

1. Introduction

Additive manufacturing (3D printing) is being increasingly applied to a wide range of applications due to advantages in fabricating complex architectures that were previously not possible or challenging to make, and producing structures with increased customisation [1,2]. Desirable functionalities may arise from these architectures produced by 3D printing. The ability of precisely controlling architecture with reproducibility has made 3D printing a very useful technology for making tissue engineered scaffolds [3]. Various 3D printing technologies have been used to fabricate scaffolds. Extrusion-based 3D printing may be arguably the most widely used technique in the tissue engineering field due to its relatively cheap equipment cost. A range of materials including polymers and hydrogels with or without encapsulated cells can be 3D printed using this technique [2,4–13]. 3D thick constructs with control over internal and external architectures can be built relatively quickly.

Previous studies on 3D printed polymeric scaffolds have investigated scaffold architectural parameters such as pore size, porosity and interconnectivity [2,4–7,14,15].

For example, the *in vivo* regeneration of the articular surface of a synovial joint has been demonstrated by using polymer scaffolds with 200-400 μm pores [14]. However, the strand surfaces of 3D printed scaffolds are usually smooth. There are a few reports on introducing topographical cues onto the strand surface of 3D printed scaffolds [16–18]. However, the roughened or patterned micro-porous surfaces still do not represent the nanostructures of extracellular matrix (ECM). Effects of nano-scale topography on cell behaviour have been extensively studied *in vitro* on 2D substrates with nano-scale topographies [19,20]. The nanotopography is involved in modulating initial cell adhesion and eventually defines cell fate through changes in cell biochemistry and cell morphology [21].

Different technologies have been used to fabricate scaffolds with nanofibrous morphology. Electrospinning has been used to create sheets of nanofibres [22–24]. However, using this technology to rapidly fabricate integrated structures over centimetre scales with defined architectures has been difficult. Thermally-induced phase separation (TIPS) has also been developed to fabricate ECM-like nanofibrous scaffolds/matrices [25,26]. The technique relies on quenching of polymer solutions, yielding the formation of polymer-rich domains which are immobilised by gelation, glass transition or crystallisation [27]. 3D printing was previously used to create a sacrificial mould for casting of a polymer solution by means of TIPS, allowing the fabrication of defined internal architectures [28,29]. However, the extra steps for making a mould and subsequent mould removal using a series of chemical solvents increase the cost, time, and complexity of the process and risks leaving residual mould materials on the strand surfaces. 3D printing of polymer solution into a low temperature chamber to allow the solidification of the solvent and subsequent TIPS process to occur has been previously demonstrated. However, only micro-porous strands were created, and the low temperature requirement restricts the choice of solvent and increases the complexity of hardware [30].

Herein, we have developed a direct fabrication approach to create 3D printed poly(L-lactide) (PLLA) scaffolds consisting of nanofibrous strands and interconnected pores by combining extrusion-based 3D printing with TIPS. Self-supporting structures with disparate features spanning from nanometres to centimetres were successfully printed at room temperature. The optimal parameters were identified to obtain continuous and uniform strands of PLLA gels during 3D printing. Enhanced fibronectin absorption, MSC adhesion and chondrogenic differentiation *in vitro* was found in the 3D nanofibrous scaffolds when compared to those with a smooth surface. Adding hydroxyapatite nanoparticles (nHA) into nanofibrous strands improved mechanical properties of the scaffolds and induced osteogenic differentiation.

2. Materials and Methods

2.1. Preparation and characterisation of polymeric gels

Polymeric gels were prepared from polymer solutions based on the TIPS technique [25]. PLLA (85-160 kDa) or PLLA/ hydroxyapatite nanoparticles (nHA, <200 nm particle size) from Sigma-Aldrich (UK) was dissolved in tetrahydrofuran (THF, Fisher Scientific, UK). Homogeneous solutions/dispersions were then loaded into syringes for 3D printing or a custom-made polytetrafluoroethylene (PTFE) mould for casting and quenched at 4^{o}C or -20^{o}C for different times.

The rheological properties of the PLLA gels were measured using a rotational rheometer (Anton Paar Physica MCR 301, UK) with a parallel plate setting (25 mm-diameter). An amplitude sweep (a strain ramp from 0.01% to 100% and a frequency of 1 Hz) was carried out to determine the linear viscoelastic region of the samples. The viscosity of the gel (n = 5) was measured in rotation mode and a shear rate ramp from 0.1 to 100 s^{-1}. Viscosity values at a

shear rate of 0.1 s^{-1} were plotted against different gelation times to obtain the gelation kinetics of the PLLA gels.

The extrusion test was performed by extruding gels into a glass cylinder (5ml) with controlled dispensing rates using a syringe pump (Cole-Parmer, UK). The degree of syneresis (n = 6) was quantified by $(v_s/v_i) \times 100\%$ where v_s is the volume (ml) of the squeezed-out THF solvent prior to achieving a continuous PLLA gel strand and v_i is the total initial gel volume (ml).

2.2. Manufacture of 3D scaffolds

Scaffolds were designed by BioCAD software and fabricated using an extrusion-based 3D printer (RegenHU, Switzerland). Smooth flow tapered tips (410-840 μm internal diameter, Adhesive Dispensing, UK) were used. For scaffolds with nanofibrous surfaces, the PLLA or PLLA/nHA gel in a printing cartridge (Adhesive dispensing), prepared from TIPS of 7.5% (w/v) PLLA/THF at -20^{o}C, was printed with a speed of 18 mm/s and a dispensing rate of 1.0 ml/min. After printing, the scaffolds were immediately immersed in cold ethanol/water mixture (70/30 v/v) for 24 h to allow solvent exchange, followed by freeze-drying. Scaffolds with a smooth surface were created by direct 3D printing of viscous PLLA/dichloromethane (DCM) solutions using a pressure of 4 bar and a printing speed of 4 mm/s. The viscosity of the solution was increased to the printable range, a viscosity value of approximately 100 Pa·s at a shear rate of 100 s^{-1} (Figure S1), by evaporation.

2.3. Characterisation of the nanofibrous topography

The topographies of scaffolds, diameters of printed strands and nanofibres, and pore sizes (edge-edge gaps between the strands) were visualised using a scanning electron microscope (JEOL JSM-6490LV, UK). Chemical compositions of the scaffold surfaces were analysed using an energy dispersive X-ray analyser (EDS, Oxford Instrument INCA, UK). For

the SEM imaging of cell morphology in MSC-seeded scaffolds, the specimens were fixed in 2.5% glutaraldehyde, post-fixed in 1% osmium tetroxide, dehydrated in increasing concentrations of ethanol followed by chemical drying with hexamethyldisilazane prior to gold sputter coating (Leica EM SCD005, UK) and SEM observation. Diameters of the nanofibres (100 fibres) were analysed by ImageJ software (NIH, USA) using SEM images at 20,000x magnification (n = 3).

2.4. Micro-computed tomography (μCT)

3D printed scaffolds were characterised using an x-ray μCT scanner (Skyscan 1172, Belgium) with an x-ray source current of 800 μA and voltage of 50 kV. Images were recorded every 0.400^{o} of rotation thorough 360^{o}. Cell infiltration studies were conducted following the previously described protocols [5,31]. In brief, cell-seeded and cell-free scaffolds (as negative controls) were fixed in 3% glutaraldehyde, stained with 1% osmium tetroxide, and dehydrated in graded ethanol concentrations prior to scanning. 2D reconstructed image slices were generated using NRecon software. The 3D-morphometric analysis of bulk porosity of the scaffolds and the reconstruction of 3D models showing pore interconnectivity and cell distribution inside 3D scaffolds were conducted using a CTAn software by thresholding the scaffolds and cells with lower grey 15 upper grey 90 and lower grey 172 upper grey 255, respectively.

2.5. Compressive testing

The compressive mechanics were measured with a Universal Texture Analyser (TA-HD Plus, Stable Microsystems, USA). The scaffolds were compressed in the z-direction with a speed of 0.5 mm/s to the strain of 0.5. The compressive modulus was calculated from a stress-strain curve using a linear slope (the strain ranging from 0.1 to 0.2). At least three specimens ($n \geq 3$) were tested for each sample.

2.6. Thermogravimetric Analysis

Thermogravimetric analysis (n =2) was performed on a Discovery TGA (Thermal Analysis Instruments, UK) in a nitrogen atmosphere with a heating rate of 10^{o}C/min.

2.7. Fibronectin absorption

Fibronectin absorbed to 3D printed scaffolds was evaluated under standard cell culture condition (37^{o}C, 5% CO_2). The scaffolds were wetted in ethanol for 30 min and then washed in phosphate-buffered saline (PBS) for 30 min twice. After incubation with PBS overnight, the scaffolds were incubated in 30 µg/ml fibronectin (Sigma-Aldrich, UK) solution in PBS. This concentration corresponds to the concentration of fibronectin in standard tissue culture medium that contains 10% FBS [32]. After 24 h incubation, a residual amount of fibronectin in the protein solution was measured with a Quick Start™ Bradford Protein Assay (Bio-Rad, UK). The amount of absorbed fibronectin was calculated by subtracting the initial amount of fibronectin with a residual amount in the protein solution. All samples and standards were done in triplicate.

2.8. Cell culture and seeding

Human mesenchymal stem cells (MSCs) were immortalised using a previously published protocol [33]. Both 3D nanofibrous and smooth-surface scaffolds were sterilised by soaking in 70% ethanol for 30 min, washed three times in PBS and twice in expansion medium (Dulbecco's modified Eagle's medium (DMEM) with 10% FBS, 1% non-essential amino acids, 1% L-glutamine and 1% antibiotic/antimycotic solution). 4 x 10^6 cells were manually seeded onto each scaffold. Three hours after seeding, either the expansion medium, chondrogenic differentiation medium (serum-free expansion medium supplemented with 50 µg/ml L-ascorbic acid phosphate, 40 µg/ml L-proline, 1% ITS+, 1 mM pyruvate and 10 ng/ml TGF-β_1, all from Invitrogen, UK) or osteogenic differentiation medium (αMEM

supplemented with 10% FBS, 1% L-glutamine and 1% antibiotic/antimycotic solution, 10 mM β-glycerophosphate and 100 nM dexamethasone) was added. The medium was changed twice a week.

2.9. Characterisation of chondrogenic differentiation

After 1, 7, 21 and 28 days of cultivation, MSC-seeded scaffolds were harvested, carefully washed with PBS and individually digested in 1 ml papain digestive solution (280 µg/ml papain, 50 mM EDTA, 5 mM L-cysteine in Dulbecco's PBS pH 6.5, all from Sigma-Aldrich) at 65ºC overnight. Digested samples were centrifuged and the supernatants were assayed for the cell numbers by total DNA quantification using a Quant-iT^{TM} Picogreen® kit (Invitrogen). Sulfated glycosaminoglycan (sGAG) content was measured using 1,9-dimethymethylene blue (DMMB, Sigma-Aldrich). Collagen content was measured using the acid hydrolysed papain digestion solution and a hydroxyproline assay kit (Sigma-Aldrich). The total collagen content was quantified from the hydroxyproline content as described previously [34]. All samples and standards were done in triplicate. Cell-free scaffolds and ovine cartilage harvested from femoral condyles of sheep were used as controls. Immunostaining of type II collagen was performed using primary antibody (Abcam, ab185430) and secondary antibody labelled with Alexa Fluor 488 (Abcam, ab150133). The sections were counterstained with Hoechst 33258 (Sigma-Aldrich) for nuclei staining and imaged using a Leica TCS LSI confocal microscope.

2.10. Characterisation of osteogenic differentiation

MSC-seeded scaffolds were harvested after 1, 7, 14 and 28 days of cultivation, washed with ice-cold PBS and individually homogenised in RIPA lysis buffer containing Halt^{TM} protease inhibitor cocktails (both solutions from Thermo Scientific, UK). Three freeze-thaw cycles were then performed to promote cell lysis. Enzymatic activity of alkaline phosphatase

(ALP) was detected using the clear supernatants from cell lysates and an ALP fluorometric assay kit (Source Bioscience, UK). Osteocalcin production was analysed using a human osteocalcin sandwich ELISA kit (Invitrogen) and following the manufacturer's protocol. All samples and standards were done in triplicate. Cell-free scaffold samples were used as negative controls.

2.11. Statistical analysis

All values in this study were reported as mean or mean ± standard deviation (SD). Statistically significant differences between two groups and more than 2 groups of the data were analysed using Wilcoxon rank-sum test and One-way ANOVA with Tukey's post hoc test, respectively. An alpha value of 0.05 was used in both methods.

3. Results and Discussion

3.1. Viscosity and gelation of PLLA gels

Since a suitable viscosity range is a predictor for successful extrusion-based 3D printing [35], the viscosity of the PLLA gel was investigated against a consecutive increase of shear rate. During the gelation process induced by TIPS, we noticed an increase in PLLA gel viscosity over time (Figure 1a and Figure S2). Lower temperature induced a quicker gelation. However, the final equilibrium viscosity was independent of gelation temperature and increased with the concentration of PLLA (approximately 20 Pa·s for 5%, 400 Pa·s for 7.5% and 1200 Pa·s for 10% (w/v)). The gelation time required to reach the final equilibrium viscosity was approximately 30 min, 10 min and 5 min for 5%, 7.5% and 10% (w/v) PLLA/THF, respectively. By visual observation, the gels did not show physical changes after 3 days at room temperature (data not shown). High concentration of PCL also formed gels at 4°C and -20°C (Table S1). However, the gels liquefied at room temperature rapidly, and

consequently may be printable at lower temperatures. The subsequent experiments use PLLA gels which were stable at room temperature for printing.

3.2. Extrusion of PLLA gels

The stability of the PLLA gel under pressure during extrusion 3D printing is critical for forming a uniform and continuous strand. During extrusion-based 3D printing, gels are squeezed through a small nozzle. Solvent can be squeezed out the polymer gel (termed "syneresis") by forces generated during the process. At 7.5% (w/v) PLLA/THF, the syneresis occurred at the beginning of the extrusion-based 3D printing process, then the remaining gel formed a continuous and uniform gel strand, allowing the formation of self-supporting 3D structures. The PLLA gels showed different degrees of syneresis depending on the dispensing rates (Figure 1b), the cartridge geometries used for loading the gels (Figure 1c) and tip diameter (Figure 1d). The degree of syneresis, in general, was lower (≤ 10%) when a higher dispensing rate was applied (Figure 1b). Syneresis occurred mostly at the junction between the syringe barrel and the syringe tip, where the cross-section reduced sharply (the inset of figure 1b). The increase in forces associated with higher barrel-to-tip ratio in cross-sectional area during extrusion may be the reason for the increased syneresis; the cohesion between PLLA molecules and the solvent in the gels is likely to be weak and susceptible to dissociation caused by external forces. As a smaller barrel-to-tip change in cross-sectional area showed a lesser amount of syneresis during extrusion (Figure 1c), small commercially available syringes (2-3 ml size) were used for 3D printing. At room temperature, 18G tapered tips were the smallest for allowing the extrusion of continuous gel strands with a relatively low degree of syneresis (10%, Figure 1d). When the PLLA gel in the printing cartridge was maintained at 4^{o}C, the stability of the PLLA gel was improved as the syneresis degree of the gel extruded through 22G tips decreased from 67% to 31% (Figure 1e). In order to use smaller nozzles for increased printing

resolution, the cartridge for loading the gels may need to be modified to have a gradual barrel-to-tip change in cross-sectional area to reduce syneresis.

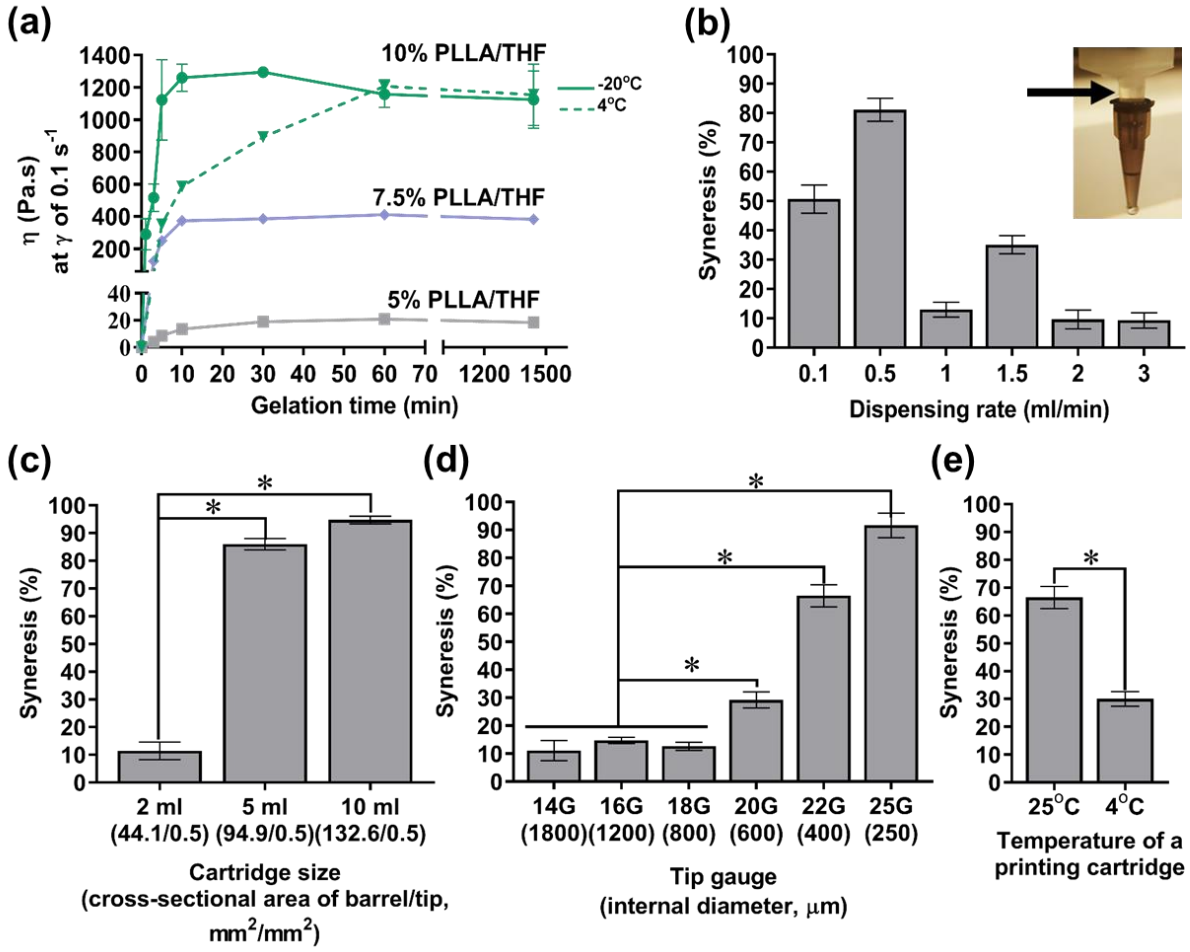

Figure 1. (a) Gelation kinetics of the PLLA gels (5%, 7.5% and 10% (w/v)) prepared from TIPS at -20°C (solid line) or 4°C (dashed line) (n = 5). Effects of (b) dispensing rate, (c) cartridge geometry, (d) tip diameter, and (e) temperature of printing cartridge on syneresis of the 7.5% PLLA gel. A 2-ml cartridge was used for (b), (d) and (e), the dispensing rate of 1.0 ml/min was used for (c), (d) and (e) and a 22G tip was used for (e). The inset of (b) shows syneresis of the gel at where the syringe cross-sectional area changes sharply. The degree of syneresis (%) was quantified by the volume of squeezed-out solvent normalized to the total starting gel volume (n = 6).

3.3. Characterisation of 3D printed scaffolds

The PLLA gel formed by TIPS was directly printed layer-by-layer with a speed of 18 mm/s to rapidly generate a 2x2x1 cm^3 self-supporting lattice structure with interconnected pores (250 µm-sized pores, 800 µm-diameter strands, 60% bulk porosity), which were confirmed by a 3D reconstruction image by µCT (Figure 2a). After printing, the gel structures were immersed in an exchange solvent to remove the THF solvent in the gels, then freeze-dried to remove the exchange solvent. The 3D printed PLLA scaffolds solidified during the process without noticeable structural shrinkage. Our developed technique is more time-efficient when compared to the previous method in which a sacrificial mould was required to be made and subsequently removed in a series of chemical solvents [28].

SEM images showed that the strand surfaces consisted of many 'broccoli-like' particles and micron-sized pores within the nanofibrous strands. Each particle was made up of many nanofibres which appeared to branch from (or converge to) a central point (Figure 2b). The nanofibrous morphology is related to lamellar branching of PLLA microcrystalline domain in THF solvent during TIPS [27,36]. These nanofibres showed diameters ranging from 50 to 450 nm (a mean diameter of 187 nm, Figure 2c), resembling the dimension of natural collagen fibrils [37]. The analysis of the surface area-to-volume ratio based on the strand surface isolated from the µCT 3D reconstructed images of the 3D printed scaffolds indicated that these nanofibrous surfaces possessed 5 times higher surface area-to-volume ratio than the smooth surfaces (0.041 μm^{-1} and 0.0084 μm^{-1} for nanofibrous and smooth surfaces, respectively). To demonstrate the feasibility of 3D printing of nanofibrous scaffolds with anatomical shapes, a model of an articular condyle was segmented from a CT image of a human long bone. The model was scaled down; the printed structure preserved relatively good fidelity compared to the 3D model (Figure S3).

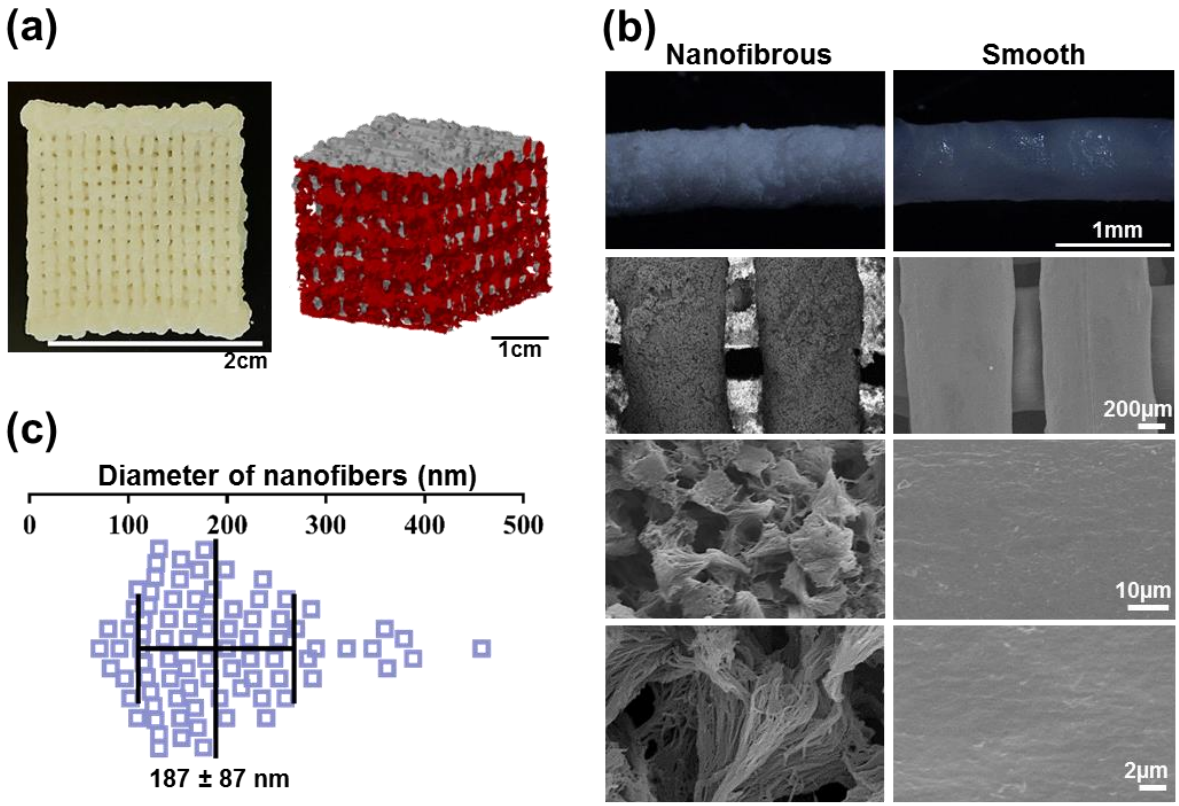

Figure 2. (a) A printed centimetre-scale porous scaffolds. The 3D reconstructed image from µCT (right) shows the interconnectivity of the pores. (b) Multi-scale images display the topography of the nanofibrous and smooth strands of 3D printed scaffolds, respectively. (c) The frequency distribution plot shows the diameter range of nanofibres (mean ± SD of 187 ± 87 nm, 100 fibres for each image, n = 3).

The nanofibrous morphology of the cast scaffolds showed a fusion of fibres on the scaffold surface; the morphology of the fibre network was different from the 3D printed strands (Figure 3). The strand diameter decreased from approximately 800 µm to 300 µm when the tip was changed from 18G to 22G. However, the nanofibres of the 3D printed strands obtained by the 22G tapered tip merged, which was different from those obtained by the 18G tip or cast scaffolds (Figure 3). The different morphologies may be caused by the difference in dimension and the effective concentration of the printed gel strands, which affected the evaporation of

solvent and consequently the gelation and formation of nanofibres. When the gels in the printing cartridge was maintained at 4°C during the printing process, the quality of the printed structure obtained from the 22G tip improved due to less syneresis of the gels during extrusion (67% to 31%, Figure 1e), and the resulting strand surfaces displayed less fusion of the nanofibres (Figure 3). This suggests the possibility of printing with higher resolution by reducing the environment temperature [30]. However, the further hardware development for controlling environment temperature is beyond the scope of this work.

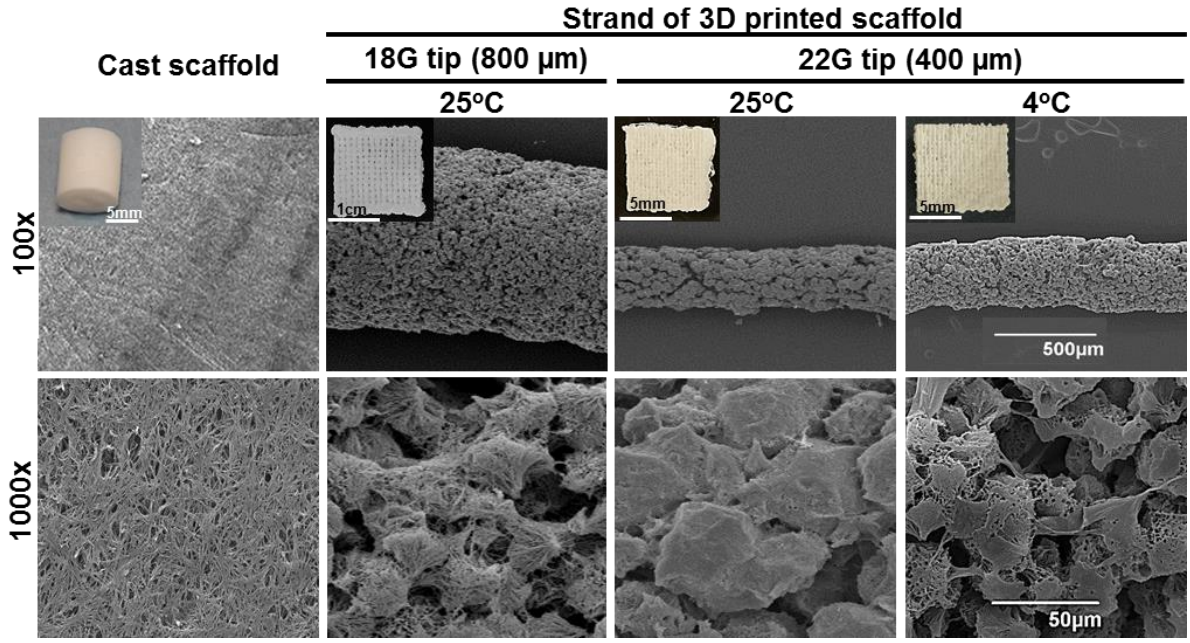

Figure 3. Topography of a cast scaffold and the strands of the 3D printed constructs using 18G or 22G tapered tips. The PLLA gel was prepared from a 7.5% (w/v) PLLA/THF solution and was maintained in a printing cartridge at 25°C or 4°C during printing.

The employed exchange solvents showed a significant effect on the surface morphology of the strands. Water produced partially fused nanofibres, whilst pure ethanol generated non-fused nanofibres (Figure 4a). Strands generated by the latter, however, were weaker and difficult to handle. We, therefore, selected 70/30 ethanol/water as the exchange solvent to

render the strands with mechanical integrity, without noticeably sacrificing the nanofibrous morphology. The PLLA gel concentration also showed a significant effect on strand topography. The 10% PLLA gel showed a completely different surface morphology (Figure 4b), in which the fibres fused, compared to the 5% (Figure 4b) and 7.5% PLLA gels (Figure 4a, the middle panel). The core of the 10% PLLA strands still showed a nanofibrous morphology (Figure S4). The difference in morphology is attributed to the evaporation of solvent which is affected by the concentration of PLLA. The evaporation was faster for PLLA gels with higher concentrations (Figure 4c).

Residual THF solvent in the nanofibrous scaffolds is biologically toxic and must be removed to render the scaffolds biocompatible. We carried out a thermogravimetric analysis (TGA) to quantify the remaining THF in the nanofibrous scaffolds after solvent exchange and freeze-drying. The pure PLLA material (without being dissolved in THF) was also analysed as a control. In comparison to the virgin PLLA, TGA profiles of the nanofibrous and composite nanofibrous scaffolds containing 70% nHA showed no weight changes within the THF evaporation temperature region (40^{o}C to 100^{o}c), suggesting no residual THF solvent in the 3D printed scaffolds after solvent exchange and freeze-drying (Figure 4d).

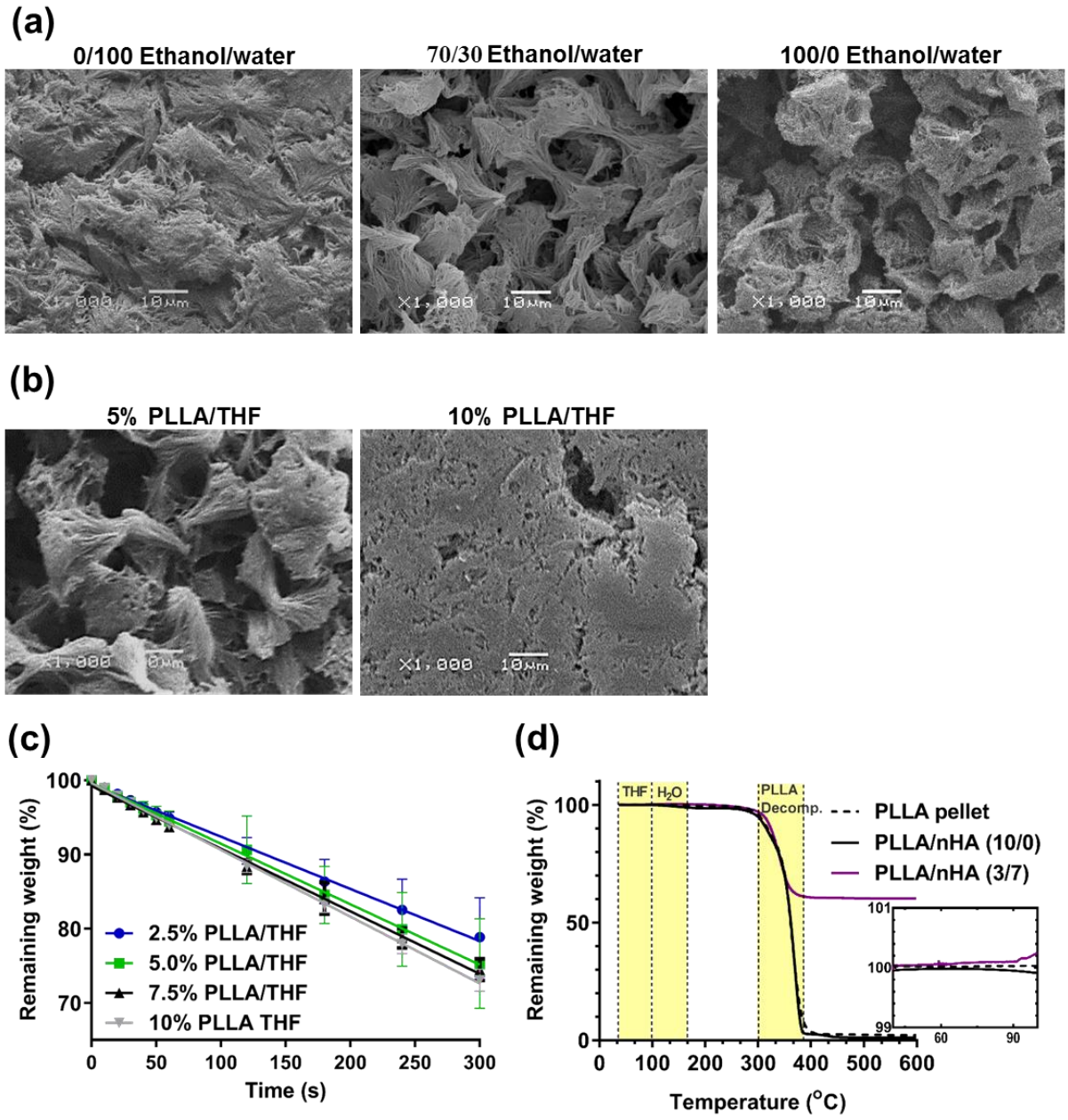

Figure 4. SEM micrographs show the effect of (a) exchanging solvent and (b) PLLA concentration on the strand topography of the 3D printed scaffolds. The concentration of PLLA for (a) was 7.5% (w/v) and the exchanging solvent for (b) was 70/30 ethanol/water. (c) THF evaporation from 2.5%, 5%, 7.5% and 10% (w/v) PLLA/THF gel represented by remaining weight (%) of the gel over 300 seconds (n = 6). (d) Thermogravimetric profiles of virgin PLLA pellet (dashed line) and nanofibrous scaffolds, after solvent exchange and freeze-drying,

containing 0% (black line) and 70% w/w of nHA (blue line). The inset shows the TGA profiles between 40^{o}C and 100^{o}C (within the THF evaporation temperature region).

3.4. MSC adhesion and proliferation inside 3D printed scaffolds

To demonstrate the advantage of nanofibrous strands, we first demonstrated improved cell proliferation and chondrogenic differentiation on 2D nanofibrous substrates when compared to the smooth surfaces (Figure S5). It is widely recognised that cells can behave differently when cultured in a 3D environment compared to 2D [38]. We then investigated the responses of MSCs within 3D printed scaffolds. 3D printed scaffolds with similar dimensions and architectural parameters (250 μm-sized pores, 800 μm-diameter strands, 60% bulk porosity) and different topographies, i.e. nanofibrous surface or smooth surface, were made, allowing the direct comparison of the impact of strand topography on MSC behaviour in a 3D environment. The 250 μm-sized pores were chosen to provide enough void space for cell movement and chondrogenic differentiation without compromising mechanical integrity of the porous scaffolds [15].

PLLA is a relatively hydrophobic material whose surface is usually modified to improve cell response [39]. A simple method was employed in this study to improve cell adhesion: after sterilising and washing, the scaffolds were immersed in serum-containing culture media overnight. Serum provides a source of cell adhesion proteins including fibronectin that plays a crucial role as mediators in cell–material surface interactions [40]. The 3D printed scaffolds with nanofibrous strands significantly enhanced fibronectin absorption in comparison with the smooth-surface scaffolds (Figure 5).

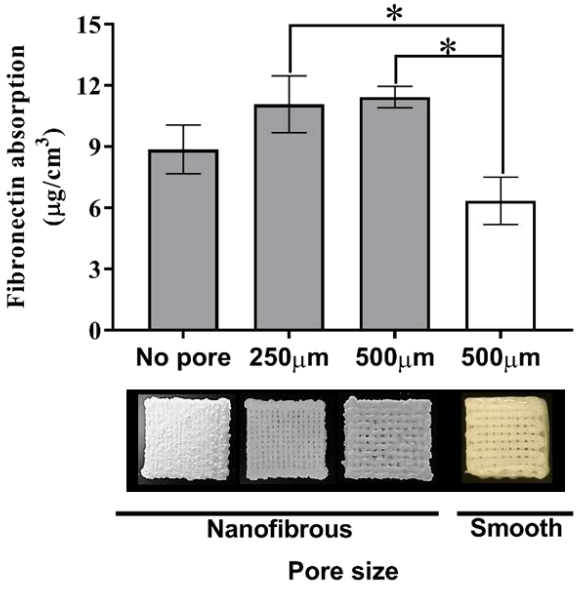

Figure 5. Amount of fibronectin absorbed to the 3D printed nanofibrous scaffolds with different pore sizes: no pore, 250 µm and 500 µm and the smooth-surface scaffold with 500 µm-sized pores (n = 3).

For the studies of cell adhesion and distribution inside 3D scaffolds, MSCs were manually seeded onto the scaffolds, and cultured for up to 28 days in expansion medium. The MSC-seeded scaffolds were then stained with osmium tetroxide and visualised by µCT with different thresholding parameters to distinguish between cells and polymeric scaffolds [5,31]. Cell-free scaffolds were also stained using the same procedure and visualised by µCT using the same thresholding parameters as the cell-seeded specimens (Figure S6). By doing this, we were confident that the cells could be differentiated from the polymer scaffolds using the µCT machine. The 2D image slices from three different heights (1, 5 and 8 mm) of both MSC-seeded 3D nanofibrous and smooth-surface scaffolds were generated (Figure 6a). All 2D µCT image slices of the nanofibrous scaffolds showed a significantly higher cell number compared to those of the smooth-surface scaffolds. As the same number of MSCs were seeded onto

nanofibrous and smooth-surface scaffolds, the higher cell numbers in the 3D nanofibrous scaffolds suggested that the nanofibrous topography improved the retention of cells, resulting in a substantially higher MSC number after 28 days (Figure 6a). The improvement of MSC adhesion on the nanofibrous 3D scaffolds compared to smooth scaffolds was in accordance with 2D flat substrates (Figure S5). The 3D μCT images demonstrated MSC distribution throughout the 3D scaffolds with higher cell density in the 3D scaffolds with a nanofibrous surface (Figure 6b). However, we observed that fewer cells resided in the central region of the nanofibrous scaffolds compared to the outer region of the bottom slice at day 28 (Figure 6a). This may be attributed to the depletion of nutrients and oxygen by cells in the outer region of the scaffold, which suggests improved design, such as graded pores [41], for large-dimension scaffolds, may be beneficial.

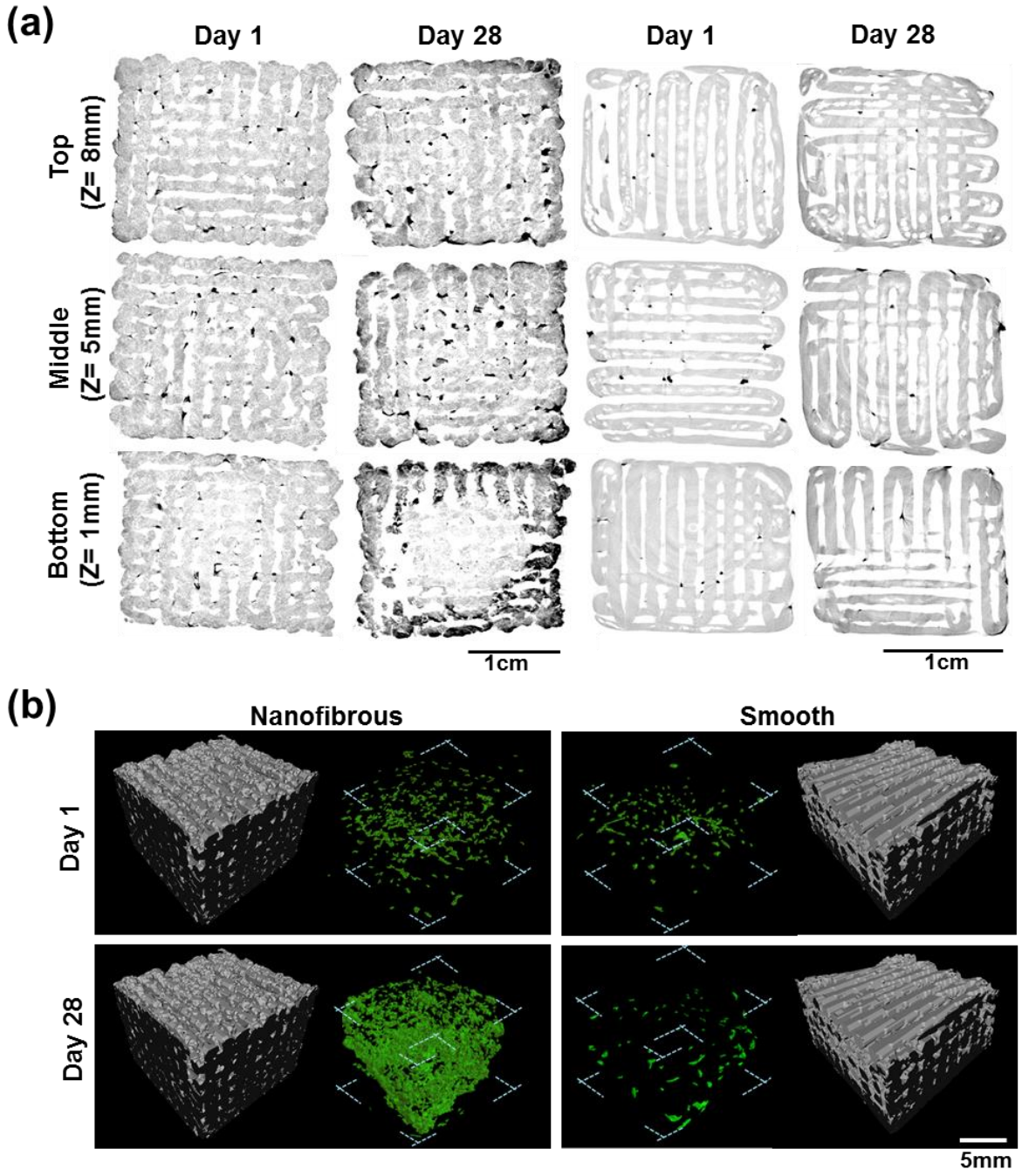

Figure 6. (a) 2D reconstructed µCT image slices of the osmium tetroxide-stained cell-seeded scaffolds showing MSC (black) adhesion on three different planes of the 3D printed scaffolds with nanofibrous or smooth surfaces. Z values indicate the height of the slice measured from the bottom of the scaffold. (b) 3D µCT images representing MSC distribution inside 3D printed scaffolds with nanofibrous or smooth surfaces. The MSCs were falsely coloured.

3.5. Chondrogenic differentiation of hMSC in 3D printed scaffolds

To demonstrate the benefit of the ECM-like topography of the 3D printed scaffolds for cartilage tissue engineering, MSC-seeded scaffolds were cultured in chondrogenic differentiation medium for up to 28 days. Compared with the smooth-surface scaffolds, total DNA content showed that the nanofibrous scaffolds exhibited significantly higher cell number at day 1, quantified by absolute DNA content (Figure 7a). MSCs proliferated at a similar rate in both 3D nanofibrous and smooth-surface scaffolds from day 1 to day 28 (inset in Figure 7a). The nanofibrous scaffold significantly boosted the production of sGAG and collagen after day 7 (Figure 7b and 7c) in comparison to the smooth-surface scaffold. At day 28, the sGAG content in the MSC-seeded nanofibrous scaffolds (40.9 ± 2.32 μg/μg DNA) reached that of articular cartilage obtained from the femoral condyles of sheep (39.24 ± 2.32 μg/μg DNA); in contrast, the collagen content (713.4 ± 179.1 μg/μg DNA) was still much lower than that of the ovine cartilage (3022.4 ± 104.8 μg/μg DNA, Figure S7). Figure 7d showed the presence of type II collagen, which is a marker of cartilage, detected by immunostaining. SEM images showed the adhesion of MSCs on the nanofibrous scaffolds at day 28. The ability to produce sGAG and type II collagen confirmed the *in vitro* formation of neo-cartilage from MSCs cultured in 3D nanofibrous scaffolds in chondrogenic differentiation medium.

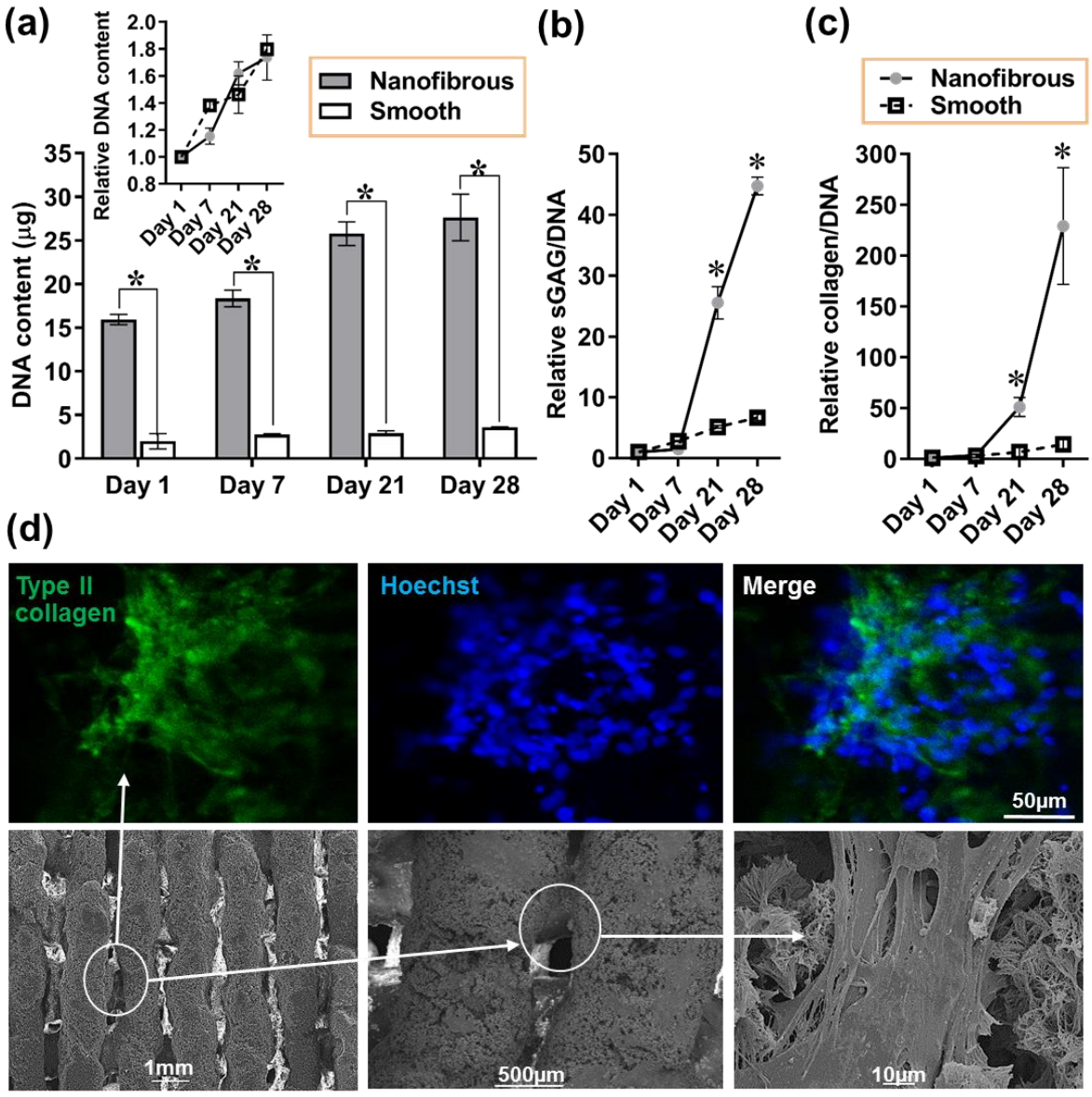

Figure 7. Chondrogenic differentiation of MSCs in 3D printed scaffolds with nanofibrous or smooth surfaces over 28 days. (a) DNA content (the inset shows relative DNA content normalized to day 1, n = 9), (b) relative sGAG content (n = 9), and (c) relative collagen content normalised to day 1 (n = 9). (d) Confocal images (Top) of type II collagen and cell nuclei and corresponding SEM images (bottom) of MSCs on the nanofibrous scaffolds cultured in the chondrogenic differentiation medium for 28 days.

3.6. Mechanical properties and osteogenesis of 3D scaffolds

Mechanical properties of the printed porous scaffolds were measured using compression testing. The compressive moduli of the nanofibrous scaffolds (250 μm-pores, bulk porosity of 8.7% and 60%) were relatively low (447 kPa and 80.4 kPa, respectively). The smooth-surface scaffolds with similar bulk porosity and pore sizes exhibited a substantially higher compressive modulus (50 MPa, Figure 8a). The pores within the nanofibrous strands were responsible for the significantly reduced modulus of the corresponding scaffolds. It has been reported that the increased surface area of nanofibrous PLLA scaffolds resulted in quicker degradation (50% vs 6% (smooth) mass loss within 15 months) due to the higher number of available sites for hydrolytic degradation [42].

Addition of hydroxyapatite nanoparticles (nHA) was found to increase the mechanical properties of the nanofibrous scaffolds (Figure 8b). With 30% and 70% content, the compressive modulus increased to 120 kPa and 1.5 MPa, respectively (Figure 8c). Human cartilage was found to possess a compressive modulus in the range of 0.44 to 20.4 MPa [43]. This means that the mechanical properties of the scaffolds can be tuned to the range of cartilage by simply adding reinforcement particles.

The introduced nHA did not affect the formation of nanofibres (Figure 8d, SEM images), which was in accordance with previous finding [44]. The nHA particles at 30% content appeared to be distributed uniformly among the nanofibers. When the nHA content was increased to 70%, the particles agglomerated to form larger particles (Figure 8d, EDS imaging of Ca) and further strengthened the scaffolds. It has been found before that nanoparticles tended to spontaneously agglomerate at high concentrations, consequently reducing their surface area and activity [44].

Interestingly, the composite surface with 70% (w/w) nHA/PLLA displayed better osteogenic differentiation of MSCs as shown by a significant increase in ALP enzymatic activity (Figure 9a) and osteocalcin production (Figure 9b), compared to scaffolds containing 0% nHA between day 7 and day 28. The presence of the hydroxyapatite nanoparticles changed the surface chemistry of the nanofibrous surfaces, which was confirmed by the chemical composition analysis (Figure 8d, EDS spectrum). The calcium concentration increased with the addition of hydroxyapatite, which resembles more closely the natural chemical composition of bone tissues [44].

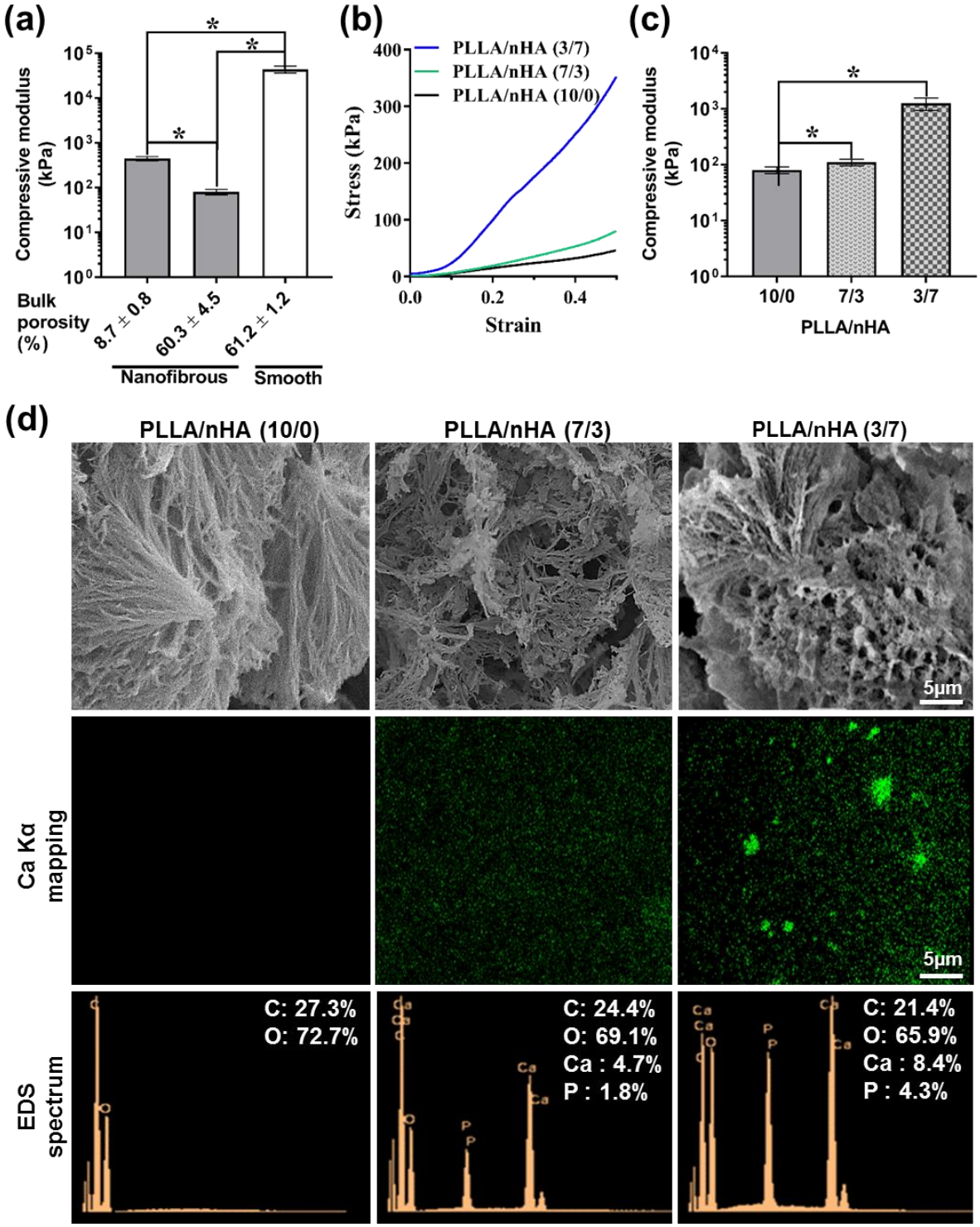

Figure 8. (a) Compressive moduli (n ≥ 3) of 3D nanofibrous scaffolds with different bulk porosities (%) and smooth-surface scaffolds. (b) Representative stress-strain curves and (c) Compressive moduli (n ≥ 3) of 3D nanofibrous scaffolds with different concentrations (w/w)

of nHA. (d) SEM images of the nanofibrous topography, EDS images of calcium and EDS spectra of the PLLA scaffolds with 0%, 30% and 70% (w/w) nHA.

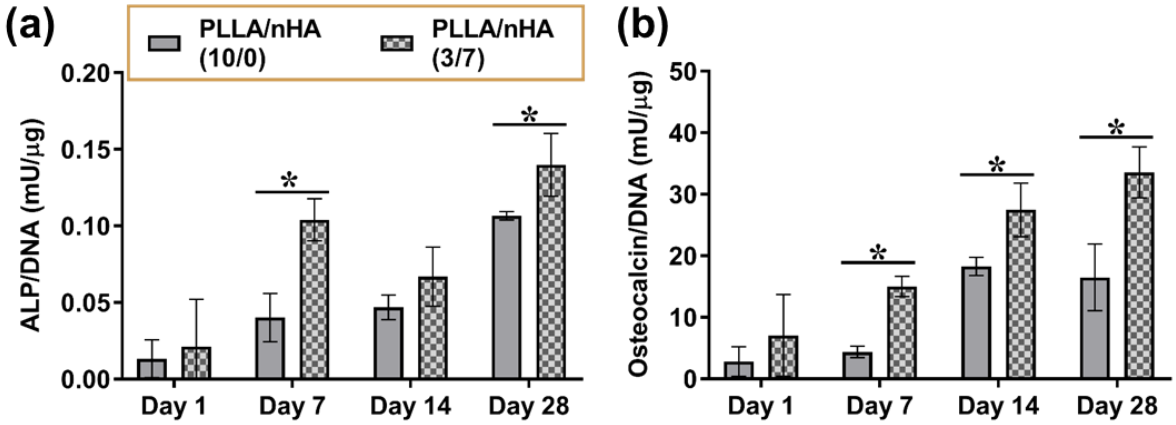

Figure 9. Osteogenic differentiation of MSCs in 3D nanofibrous scaffolds, prepared from 7.5% PLLA gel with 0% or 70% (w/w) nHA. The MSCs were characterised by relative (a) enzymatic activity of alkaline phosphatase (n = 9) and (b) osteocalcin production detected by ELISA (n = 9). MSC-seeded scaffolds were cultured in in the osteogenic differentiation medium.

4. Conclusion

We have developed a novel method for 3D printing polymer scaffolds with nanofibrous strands. Compared to previous developments in 3D printing of polymeric scaffolds, in which strands possessed a smooth surface or micro-scale topographies, the nanofibrous strands developed in this study significantly enhanced the absorption of fibronectin, the adhesion and chondrogenic differentiation of human mesenchymal stem cells. The combination of 3D printing and TIPS allowed the direct fabrication of large-dimension nanofibrous scaffolds with defined architectures, which is a simpler and more efficient approach compared to moulding, in which the sacrificial mould need removal after casting. The addition of hydroxyapatite nanoparticles improved the mechanical properties of the highly porous scaffolds and promoted

osteogenesis of MSCs. These 3D printed nanofibrous scaffolds can potentially be used in other tissue engineering applications where a collagen-like morphology and defined architectures are required.

Supplementary Data

Seven supporting figures and one table.

Acknowledgements

The authors would like to thank Dr.Jane McLaren and Laura Luiz-Cantu for μCT analysis suggestions, Dr.Mick Cooper for technical help with TGA, Pritesh Mistry for his help with macro-confocal imaging, the Development and Promotion of Science and Talent Project (DPST) for sponsoring Mr. Aruna Prasopthum's studentship and Nanoscale and Microscale Research Centre (NMRC) for electron microscope facilities.

References

[1] Chia H N and Wu B M 2015 Recent advances in 3D printing of biomaterials *J. Biol. Eng.* **9** 4

[2] Moroni L, de Wijn J R and van Blitterswijk C A 2006 3D fiber-deposited scaffolds for tissue engineering: Influence of pores geometry and architecture on dynamic mechanical properties *Biomaterials* **27** 974–85

[3] Murphy S V and Atala A 2014 3D bioprinting of tissues and organs *Nat. Biotechnol.* **32** 773–85

[4] Zein I, Hutmacher D W, Tan K C and Teoh S H 2002 Fused deposition modeling of novel scaffold architectures for tissue engineering applications *Biomaterials* **23** 1169–85

[5] Ruiz-Cantu L, Gleadall A, Faris C, Segal J, Shakesheff K and Yang J 2016 Characterisation of the surface structure of 3D printed scaffolds for cell infiltration and surgical suturing *Biofabrication* **8**

[6] Malda J, Woodfield T B F, van der Vloodt F, Wilson C, Martens D E, Tramper J, van Blitterswijk C A and Riesle J 2005 The effect of PEGT/PBT scaffold architecture on the composition of tissue engineered cartilage *Biomaterials* **26** 63–72

[7] Woodfield T B F, Malda J, de Wijn J, Peters F, Riesle J and van Blitterswijk C A 2004 Design of porous scaffolds for cartilage tissue engineering using a three-dimensional fiber-deposition technique *Biomaterials* **25** 4149–61

[8] Mistry P, Aied A, Alexander M, Shakesheff K, Bennett A and Yang J 2017 Bioprinting Using Mechanically Robust Core-Shell Cell-Laden Hydrogel Strands *Macromol Biosci*

[9] Lee C H, Rodeo S A, Fortier L A, Lu C, Erisken C and Mao J J 2014 Protein-releasing polymeric scaffolds induce fibrochondrocytic differentiation of endogenous cells for knee meniscus regeneration in sheep *Sci. Transl. Med.* **6**

[10] Luo Y X, Lode A and Gelinsky M 2013 Direct Plotting of Three-Dimensional Hollow Fiber Scaffolds Based on Concentrated Alginate Pastes for Tissue Engineering *Adv. Healthc. Mater.* **2** 777–83

[11] Tabriz A G, Hermida M A, Leslie N R and Shu W 2015 Three-dimensional bioprinting of complex cell laden alginate hydrogel structures *Biofabrication* **7** 45012

[12] Homan K A, Kolesky D B, Skylar-Scott M A, Herrmann J, Obuobi H, Moisan A and Lewis J A 2016 Bioprinting of 3D Convoluted Renal Proximal Tubules on Perfusable Chips *Sci. Rep.* **6** 34845

[13] Colosi C, Shin S R, Manoharan V, Massa S, Costantini M, Barbetta A, Dokmeci M R, Dentini M and Khademhosseini A 2016 Microfluidic Bioprinting of Heterogeneous 3D Tissue Constructs Using Low-Viscosity Bioink *Adv. Mater.* **28**677–684a

[14] Lee C H, Cook J L, Mendelson A, Moioli E K, Yao H and Mao J J 2010 Regeneration of the articular surface of the rabbit synovial joint by cell homing: A proof of concept study *Lancet* **376** 440–8

[15] Zhang Z Z, Jiang D, Ding J X, Wang S J, Zhang L, Zhang J Y, Qi Y S, Chen X S and Yu J K 2016 Role of scaffold mean pore size in meniscus regeneration *Acta Biomater.* **43** 314–26

[16] Mata A, Kim E J, Boehm C A, Fleischman A J, Muschler G F and Roy S 2009 A three-dimensional scaffold with precise micro-architecture and surface micro-textures *Biomaterials* **30** 4610–7

[17] Kumar G, Waters M S, Farooque T M, Young M F and Simon Jr. C G 2012 Freeform fabricated scaffolds with roughened struts that enhance both stem cell proliferation and differentiation by controlling cell shape *Biomaterials* **33** 4022–30

[18] Neves S C, Mota C, Longoni A, Barrias C C, Granja P L and Moroni L 2016 Additive manufactured polymeric 3D scaffolds with tailored surface topography influence mesenchymal stromal cells activity *Biofabrication* **8** 25012

[19] Dalby M J, Gadegaard N, Tare R, Andar A, Riehle M O, Herzyk P, Wilkinson C D and Oreffo R O 2007 The control of human mesenchymal cell differentiation using nanoscale symmetry and disorder *Nat Mater* **6** 997–1003

[20] McMurray R J, Gadegaard N, Tsimbouri P M, Burgess K V, McNamara L E, Tare R, Murawski K, Kingham E, Oreffo R O and Dalby M J 2011 Nanoscale surfaces for the long-term maintenance of mesenchymal stem cell phenotype and multipotency *Nat Mater* **10** 637–44

[21] Dalby M J, Gadegaard N and Oreffo R O 2014 Harnessing nanotopography and integrin-matrix interactions to influence stem cell fate *Nat Mater* **13** 558–69

[22] Li W J, Laurencin C T, Caterson E J, Tuan R S and Ko F K 2002 Electrospun nanofibrous structure: A novel scaffold for tissue engineering *J. Biomed. Mater. Res.* **60** 613–21

[23] Deshpande P, Ramachandran C, Sefat F, Mariappan I, Johnson C, McKean R, Hannah M, Sangwan V S, Claeyssens F, Ryan A J and MacNeil S 2013 Simplifying corneal surface regeneration using a biodegradable synthetic membrane and limbal tissue explants *Biomaterials* **34** 5088–106

[24] Lee J, Jang J, Oh H, Jeong Y H and Cho D-W 2013 Fabrication of a three-dimensional nanofibrous scaffold with lattice pores using direct-write electrospinning *Mater. Lett.* **93** 397–400

[25] Ma P X and Zhang R Y 1999 Synthetic nano-scale fibrous extracellular matrix *J. Biomed. Mater. Res.* **46** 60–72

[26] Holzwarth J M and Ma P X 2011 Biomimetic nanofibrous scaffolds for bone tissue engineering *Biomaterials* **32** 9622–9

[27] van de Witte P, Dijkstra P J, van den Berg J W A and Feijen J 1996 Phase separation processes in polymer solutions in relation to membrane formation *J. Memb. Sci.* **117** 1–31

[28] Chen V J, Smith L A and Ma P X 2006 Bone regeneration on computer-designed nano-fibrous scaffolds *Biomaterials* **27** 3973–9

[29] Akbarzadeh R, Minton J A, Janney C S, Smith T A, James P F and Yousefi A-M 2015 Hierarchical polymeric scaffolds support the growth of MC3T3-E1 cells *J. Mater. Sci. Mater. Med.* **26** 116

[30] Liang Y, Zheng X, Zhai W and Sun T 2012 3D PLLA/nano-Hydroxyapatite scaffolds with hierarchical porous structure fabricated by low-temperature deposition manufacturing *J. Wuhan Univ. Technol. Mater. Sci. Ed.* **27** 265–9

[31] Silva M M C G, Cyster L A, Barry J J A, Yang X B, Oreffo R O C, Grant D M, Scotchford C A, Howdle S M, Shakesheff K M and Rose F R A J 2006 The effect of anisotropic architecture on cell and tissue infiltration into tissue engineering scaffolds *Biomaterials* **27** 5909–17

[32] Hayman E G and Ruoslahti E 1979 Distribution of fetal bovine serum fibronectin and endogenous rat cell fibronectin in extracellular matrix *J. Cell Biol.* **83** 255–9

[33] Okamoto T, Aoyama T, Nakayama T, Nakamata T, Hosaka T, Nishijo K, Nakamura T, Kiyono T and Toguchida J 2002 Clonal heterogeneity in differentiation potential of immortalized human mesenchymal stem cells *Biochem. Biophys. Res. Commun.* **295** 354–61

[34] Kliment C R, Englert J M, Crum L P and Oury T D 2011 A novel method for accurate collagen and biochemical assessment of pulmonary tissue utilizing one animal *Int J Clin Exp Pathol* **4** 349–55

[35] Malda J, Visser J, Melchels F P, Juengst T, Hennink W E, Dhert W J A, Groll J and Hutmacher D W 2013 25th Anniversary Article: Engineering Hydrogels for Biofabrication *Adv. Mater.* **25** 5011–28

[36] Liu Q, Lv R, Na B and Ju Y 2015 Robust polylactide nanofibrous membranes by gelation/crystallization from solution *RSC Adv.* **5** 57076–81

[37] Kadler K E, Holmes D F, Trotter J A and Chapman J A 1996 Collagen fibril formation. *Biochem. J.* 1–11

[38] Baker B A, Pine P S, Chatterjee K, Kumar G, Lin N J, McDaniel J H, Salit M L and Simon Jr. C G 2014 Ontology analysis of global gene expression differences of human bone marrow stromal cells cultured on 3D scaffolds or 2D films *Biomaterials* **35** 6716–26

[39] Mikos A G, Lyman M D, Freed L E and Langer R 1994 Wetting of poly(l-lactic acid) and poly(dl-lactic-co-glycolic acid) foams for tissue culture *Biomaterials* **15** 55–8

[40] Ruoslahti E and Pierschbacher M 1987 New perspectives in cell adhesion: RGD and integrins *Science (80-.).* **238**

[41] Di Luca A, Ostrowska B, Lorenzo-Moldero I, Lepedda A, Swieszkowski W, Van Blitterswijk C, Moroni L, Sany J and Jorgensen C 2016 Gradients in pore size enhance the osteogenic differentiation of human mesenchymal stromal cells in three-dimensional scaffolds *Sci. Rep.* **6** 22898

[42] Chen V J and Ma P X 2006 The effect of surface area on the degradation rate of nano-fibrous poly(l-lactic acid) foams *Biomaterials* **27** 3708–15

[43] Shepherd D E T and Seedhom B B 1999 The ‘instantaneous’ compressive modulus of human articular cartilage in joints of the lower limb *Rheumatology* **38** 124–32

[44] Han W, Zhao J, Tu M, Zeng R, Zha Z and Zhou C 2013 Preparation and characterization of nanohydroxyapatite strengthening nanofibrous poly(L-lactide) scaffold for bone tissue engineering *J. Appl. Polym. Sci.* **128** 1332–8